AIAA SciTech Forum
23-27 January 2023, National Harbor, MD & Online
AIAA SCITECH 2023 Forum

10.2514/6.2023-2137

Effect of Reynolds Number on Traveling Wave Flow Control

Uchenna E Ogunka*, Amir M Akbarzadeh †, Iman Borazjani.‡
J. Mike Walker '66 Department of Mechanical engineering, Texas A&M University, College Station, TX, 77840

Large-eddy simulations (LES) of the fluid flow over a NACA0018 airfoil at AOA $= 20^\circ$ **angle of attack are performed to investigate the effect of surface morphing oscillations on the aerodynamic performance of the airfoil over a wide range of Reynolds numbers (Re =** $5,000$ **to** $500,000$**). These oscillations are in the form of low amplitude backward (opposite to the airfoil's forward motion) traveling wave actuations on the upper surface of the airfoil. The sharp interface curvilinear immersed boundary (CURVIB) method is used to handle the moving surface of the airfoil. The nondimensional amplitude is** $a^* = 0.001$ **(**$a^* = a/L; a$ **: amplitude,** L**: chord length of the airfoil) and reduced frequency (**$f^* = fL/U$**;** f **is the frequency and** U **is the freestream velocity) is chosen to match the leading edge vortex shedding frequency. The results of the simulations at the post-stall angle of attack (AOA** $= 20^\circ$**) show that the lift coefficient increases more than** 20% **and the drag coefficient decreases more than** 40% **within the Reynolds number range of** $Re = 50,000 - 500,000$ **for traveling wave actuation of amplitude,** $a^* = 0.001$**, and frequency,** $f^* = 8$**. However, the lift and drag coefficients of the actuated airfoil were similar to the baseline airfoil for** $Re = 5,000$**.**

Nomenclature

a = maximum amplitude of oscillation

a^* = nondimensional amplitude of oscillation, a/L

C = wave speed, λf

C^* = nondimensional wave speed, C/U

C_D = mean drag coefficient, $\overline{F}_D/0.5\rho U^2 L$

---

[*] PhD Candidate, J. Mike Walker '66 Department of Mechanical engineering, Texas A&M University, College Station, TX

[†] Postdoctoral Researcher, J. Mike Walker '66 Department of Mechanical engineering, Texas A&M University, College Station, TX

[‡] Associate Professor, J. Mike Walker '66 Department of Mechanical engineering, Texas A&M University, College Station, TX

C_L = mean lift coefficient, $\overline{F}_L/0.5\rho U^2 L$

δt = time step

f = frequency

f^* = reduced frequency, fL/U

$\overline{F}_D$ = mean lift force per airfoil unit span acting along the X direction

$\overline{F}_L$ = mean lift force per airfoil unit span acting along the Y direction

L = chord length of the airfoil

P = fluid pressure

Re = Reynolds number, UL/ν

s = airfoil span length, $0.1L$

U = free stream velocity

λ = wavelength

λ^* = nondimensional wavelength, λ/L

ρ = fluid density

ν = kinematic viscosity

I. Introduction

The research of flow separation management for low Reynolds number ($Re < 500,000$) [1–3] flow is critical to the aviation industry. At low Reynolds number and angles of attack (AOA) over the stall angle, flow separation of the laminar boundary layer from the upper surface of the airfoil may result in a sharp fall in lift and increase in drag [2–6]. Recent breakthroughs in flow separation control research, inspired by aquatic swimmers, have demonstrated that innovative traveling wave surface morphing actuators might increase the aerodynamic performance of airfoils at stall and post-stall AOA [7–13]. These traveling waves are generated using piezoelectric actuators that are fixed along the upper surface of the airfoil [7, 10–12, 14, 15]. At stall angle (AOA = 15°) and Re = $50,000$, Akbarzadeh and Borazjani [10] observed that traveling waves significantly reduce drag, increase lift, and minimize flow separation. This is due to the fact that traveling waves diminish flow separation by triggering flow instabilities and directly injecting fluid flow momentum in the streamwise direction. In contrast to standing waves (flow control mechanism is only by triggering instabilities), traveling waves have been shown to perform better [8, 10, 16]. Ogunka et al., [7–9, 16] numerically investigated the role of frequency, amplitude and starting location of oscillation of traveling waves at stall and post-stall ($\text{AOA} = 15° - 20°$) and $\text{Re} = 50,000$, and observed an improvement in aerodynamic performance (lift enhancement and drag reduction), stall suppression, and flow reattachment at the amplitude range $0.001 \leq a^* \leq 0.004$ at reduced frequency range $f^* = 8 - 12$.

The findings showed that for $\text{Re} = 50,000$, the traveling wave surface actuation can increase aerodynamic performance and minimize flow separation of an airfoil at stall and post-stall angles of attack. The prior research, however, gave little attention to the influence of Reynolds number on the flow behavior and aerodynamic performance of the airfoil above the stall angle of attack ($\text{AOA} \geq 18°$). Thompson et al., [13] observed that at $Re = 1,000$ and $\text{AOA} = 15°$, traveling waves with amplitude range of $(0.01 \leq a^* \leq 0.05)$ produced significant lift enhancement compared to the baseline (unactuated) flow for a stalled NACA0012 airfoil. Kang et al., [5] also observed significant lift enhancement for periodic excitations with a range of amplitude of $(0.5 \leq a^* \leq 1.0)$ at $Re = 5,000$ and $\text{AOA} = 6°$ for a NACA0012 airfoil. However, the amplitudes tested are higher than the range of amplitudes of experimental traveling wave oscillations that can be generated from piezoelectric actuators $(2 \times 10^{-3} > a^* > 6 \times 10^{-5})$ [12, 14]. Therefore, lower amplitudes of traveling wave oscillations need to be tested. Moreover, Sato et al., [17] observed that for flows within the Reynolds number range of $50,000 \leq Re \leq 200,000$, an important mechanism for flow reattachment was the transition of the laminar boundary layer to turbulence. This suggests that effective flow control methods for flows of $10^3 \leq Re < 0.5 \times 10^6$ may not work for flows of higher Reynolds number $Re \geq 0.5 \times 10^6$ where the boundary layer is already turbulent. Hence, a different strategy for flow control methods would be required for separated turbulent flows [17–20]. Hence, the purpose of this study is to investigate the influence of Reynolds number on the flow behavior and aerodynamic performance (lift and drag) of the NACA0018 airfoil at post-stall angle of attack ($\text{AOA} = 20°$) throughout a wide range of Reynolds number, $\text{Re} = 5,000 - 500,000$.

This paper is organized as follows: the governing equations, computational grid details, and numerical approaches are described in Section II. The mean lift and drag coefficients of the NACA0018 airfoil are measured to determine its aerodynamic performance. The actuated NACA0018 airfoil's lift and drag coefficients are compared to the baseline NACA0018 airfoil at $\text{AOA} = 20°$ and $\text{Re} = 5,000 - 500,000$ (Section III). The flow characteristics of the NACA0018 airfoil are examined by viewing the spanwise vorticity flow field (Section III). Finally, the results are reviewed, and the conclusion is described in Section IV.

II. Method

Numerical simulations of a NACA0018 airfoil at different Reynolds numbers ($Re = UL/\nu = 5,000 - 500,000$: U is the free stream velocity, L is the chord length of the airfoil, and ν is the kinematic viscosity) are compared. The simulation structure and numerical approach used to solve the issue are similar to those described in our earlier works [7, 9–11]. Using a specified local frame (X, Y, Z), a new position of the upper surface of the airfoil under motion in the original Cartesian frame (x, y, z) is computed (i.e. its origin is at the leading edge and is rotated by the angle of attack, shown in Fig. 1b).

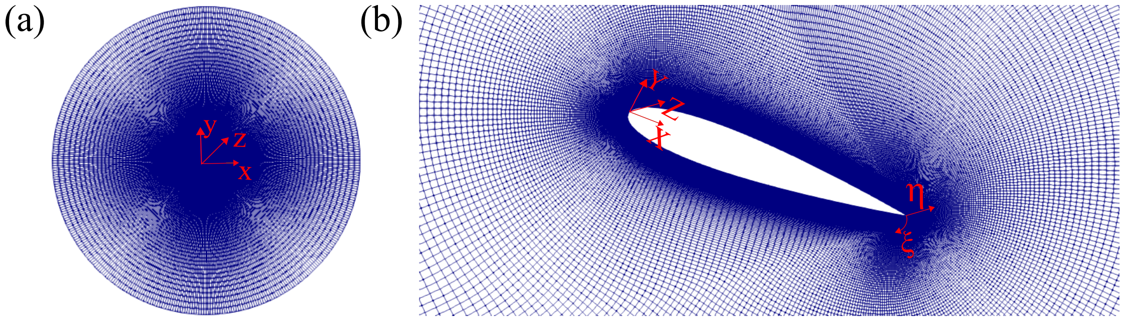

Fig. 1 (a) Computational O-grid mesh domain and (b) the simulation setup with the O-grid mesh around the NACA0018 airfoil [16].

The backward traveling wave ($h(X,t)$) prescribed along the Y direction is:

$$h^*(X,t) = a^*(X)\sin(2\pi(f^*t^* - X^*/\lambda^*)), \tag{1}$$

where $h^* = h/L$ is the nondimensional displacement of the upper surface, $f^* = fL/U$ is the reduced frequency, $\lambda^* = \lambda/L$ is the nondimensional wavelength, $t^* = tU/L$ is the nondimensional time, $X^* = X/L$ is the nondimensional streamwise length that begins at the leading edge, and $a^*(X) = a(X)/L$ is the nondimensional amplitude of the wave which starts from $X = 0.1L$ from the leading edge, to $X = 0.85L$ towards the trailing edge. The amplitude is equal to the maximum amplitude (a^*_{max}) from $X = 0.1L$ to $X = 0.8L$ and decreases linearly toward the trailing edge. The backward traveling wave moves from the leading edge to the trailing edge with a nondimensional wave speed, $C^* = f^*\lambda^*$. Here, the parameters with (*) sign are nondimensional in this case.

The flow governing equations are the filtered, unsteady, incompressible, three-dimensional Navier-Stokes and continuity equations. The flow governing equations are spatially discretized using a second order central scheme [21] and temporally integrated with a second-order fractional-step approach [22]. The momentum equations are solved using the Newton-Krylov technique and an approximate analytical Jacobian solver [23], while the pressure Poisson equation is solved using GMRES solver with a multigrid preconditioner [22]. The computational solver is fully parallelized using massage passing programming (MPI) and Portable, Extensible Toolkit for Scientific Computation (PETSc) libraries [24].

The moving boundaries are handled using the sharp interface curvilinear immersed boundary method (CURVIB), as described in prior publications [22, 25, 26]. The background mesh is fixed and the fluid points near the moving boundaries (immersed nodes) have their velocities reconstructed via an interpolation along the normal to the surface. At the moving boundaries, a no-slip boundary condition is prescribed. The domain is classified into solid, immersed, and fluid nodes using a ray-tracing algorithm technique [27]. The CURVIB method has been validated for flows with moving boundaries [27] and has been used in simulations involving turbulent flow [28], and biological flows such as aquatic locomotion [29, 30], cardiovascular flows [25, 31–33] and aneurysm blood flow [34, 35]

The turbulent flow is modeled using the large eddy simulation (LES) approach. The subgrid stress tensor is computed using a dynamic subgrid-scale model [36]. Previous studies [37, 38] have demonstrated that subgrid-scale models are suitable for modeling transitional turbulent flows. The flow over the baseline airfoil is fully separated such that it automatically transforms into a turbulent flow. The LES of the baseline case was run until it achieved a quasi-steady state. The LES method approach has been validated for simulating transitional and turbulent flows, such as inclined plates [39], wall-bounded flows [21, 39, 40] and vortex flow applications [28]. The LES of the fully developed turbulent channel [40] confirmed that our LES can resolve the mean flow and turbulent statistics of turbulent boundary layers. Further information on the LES modeling can be found in previous studies [26, 40].

The computational grid detail is the same as previous study [7–10, 16], as shown in Fig.1. The grid of the fluid domain is an O-grid mesh, which is generated in curvilinear coordinates (ξ, η, ζ), where ξ is parallel to the airfoil surface and η is normal to the airfoil surface. For $Re = 5,000 - 50,000$, the resolution of the grid is $421 \times 281 \times 21$ in the (ξ, η, ζ) direction. For $Re = 500,000$, the grid reolution is $677 \times 445 \times 41$ in the (ξ, η, ζ) direction. To generate a 3D grid domain, the grid is extruded in the ζ direction for $0.1L$. The O-grid mesh depicted in Fig. 1a has a radius of $15L$. Fig. 1b shows a zoomed-in view of the grid close to the airfoil. Periodic boundary conditions are prescribed along the ξ and ζ axes. On the outer boundary η, the upstream is described by an inlet velocity ($u_X = U$) at $X < 0$, whereas the downstream is characterized with a Neumann boundary condition with a mass flux correction at $X > 0$. To resolve the viscous boundary layer, the grid resolution is kept at $0.0002L$ for $Re = 5,000 - 50,000$ and $0.00004L$ for $Re = 500,000$ along η direction with a wall unit spacing of $\eta^+ \leq 1.0$ ($\eta^+ = \delta_\eta u_\tau/\nu$; δ_η is the normal distance between the first fluid node and wall surface, and u_τ is the friction velocity). The grid spacing is constant until $\eta = 0.022$, after which it increases with a hyperbolic function towards the boundaries. The time step is $0.0003L/U$ for the baseline and actuated airfoil simulations at 20°. The time step values correspond to the Courant–Friedrichs–Lewy (CFL) number, $CFL = U\delta t/\Delta x \leq 0.5$. More information on the validation and grid sensitivity can be found in our previous studies [10, 11, 16].

The aerodynamic performance of the NACA0018 airfoil is measured by analysing the mean lift coefficient $\overline{C}_L = \overline{F}_L/0.5\rho U^2 L$ and mean drag coefficient $\overline{C}_D = \overline{F}_D/0.5\rho U^2 L$. They are calculated by averaging the final $40,000$ iterations which corresponds to about 40 time units (t^*) reported in table 1. $\overline{F}_L$ is the mean force per unit airfoil span along the y direction, $\overline{F}_D$ is the mean force per unit airfoil span along the x direction, and ρ is the density of the fluid.

III. Results

In this section, the aerodynamic performance (lift and drag) of the baseline and actuated NACA0018 airfoil cases (Table 1) are investigated and discussed in Subsection III.A at AOA = 20° and $Re = 5,000 - 500,000$. The wavelength is constant at $\lambda^* = 0.44$, the same as the experimental study of Olivett et al. [12, 14]. Cases $1, 4^*$ and 6 are the baseline (unactuated) airfoil at $Re = 5,000, 50,000$ and $500,000$, respectively. Cases $2 - 3, 5^*$ and 7 are the actuated airfoils with backward surface morphing traveling waves with amplitude of $a^* = 0.001$ for $Re = 5,000, 50,000$ and $500,000$, respectively.

Fig. 2a-b represents the power spectrum of the frequency domain for the baseline airfoil at Re = $50,000$ and Re = $500,000$, respectively. It is calculated by spectrum analysis of the streamwise velocity, u_x, for total nondimensional time of $t^* = 220$, at a location near the leading edge, i.e., at $X = 0.086L$ and $Y = 0.28L$ with respect to the leading edge $(X, Y = 0, 0)$ (Fig. 1b). Fig. 2a and b show that the vortex shedding frequency of the leading edge shear layer is within the range of $f^* = 6$ to $f^* = 10$ at Re = 50,000 and $f^* = 7$ to $f^* = 12$ at Re = 500,000. It was observed in our previous work that low amplitude ($a^* = 0.001 - 0.002$) traveling wave actuation, with the reduced frequency of $f^* = 8 - 12$ (within the range of the leading edge vortex shedding frequency), significantly improved the aerodynamic performance (lift enhancement and drag reduction) and reattached the flow [7–9, 16]. Hence, the reduced frequency of the traveling wave surface actuation is chosen to be within the range of the leading edge vortex shedding frequency. The baseline airfoil is represented by the first, fourth, and sixth cases, with Re = $5,000, 50,000$ and $500,000$, respectively in table 1. The second, third, fifth and seventh cases are actuated airfoils with backward traveling waves with amplitude $a^* = 0.001$ at Re = $5,000, 50,000$ and $500,000$, respectively, in table 1.

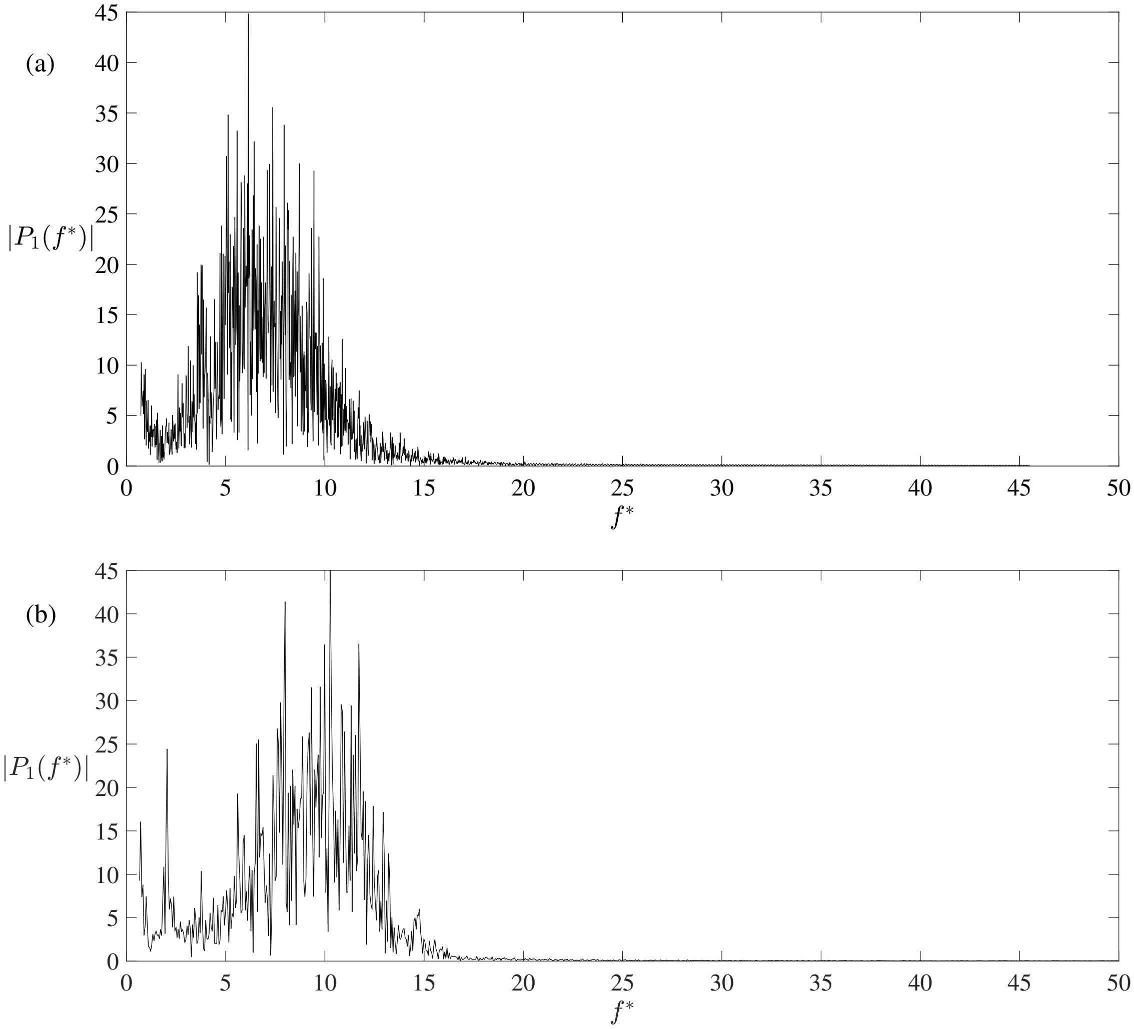

Fig. 2 The plot of the power spectrum of the velocity (P_1) in the frequency domain for baseline airfoil at (a) Re = $50,000$ and (b) Re = $500,000$ near the leading edge at post-stall. Figure 2(a) is from the previous publication [7, 16].

Table 1 The case studies, including baseline airfoil, backward traveling actuations with reduced frequency (f^*), and different Reynolds number (Re). The nondimensional amplitude (a^*) and angle of attack is kept constant at $a^* = 0.001$ and AOA $=20^\circ$, respectively. C_L and C_D are the mean lift and drag coefficients, respectively. Here, cases with $(*)$ are from the previous work of Ogunka et al., [9, 16].

Case	Wave Type	f^*	a^*	Re	C_L	C_D	$\sigma(C_L)$	$\sigma(C_D)$	AOA
1	Baseline	−−	−−	5,000	0.63	0.35	0.0097	0.0028	20°
2	Backward traveling wave	0.6	0.001	5,000	0.68	0.30	0.0108	0.0027	20°
3	Backward traveling wave	8.0	0.001	5,000	0.68	0.32	0.0108	0.0027	20°
4^*	Baseline	−−	−−	50,000	0.70	0.31	0.1701	0.057	20°
5^*	Backward traveling wave	8.0	0.001	50,000	0.87	0.17	0.1430	0.048	20°
6	Baseline	−−	−−	500,000	0.71	0.30	0.2241	0.064	20°
7	Backward traveling wave	8.0	0.001	500,000	1.00	0.16	0.1701	0.081	20°

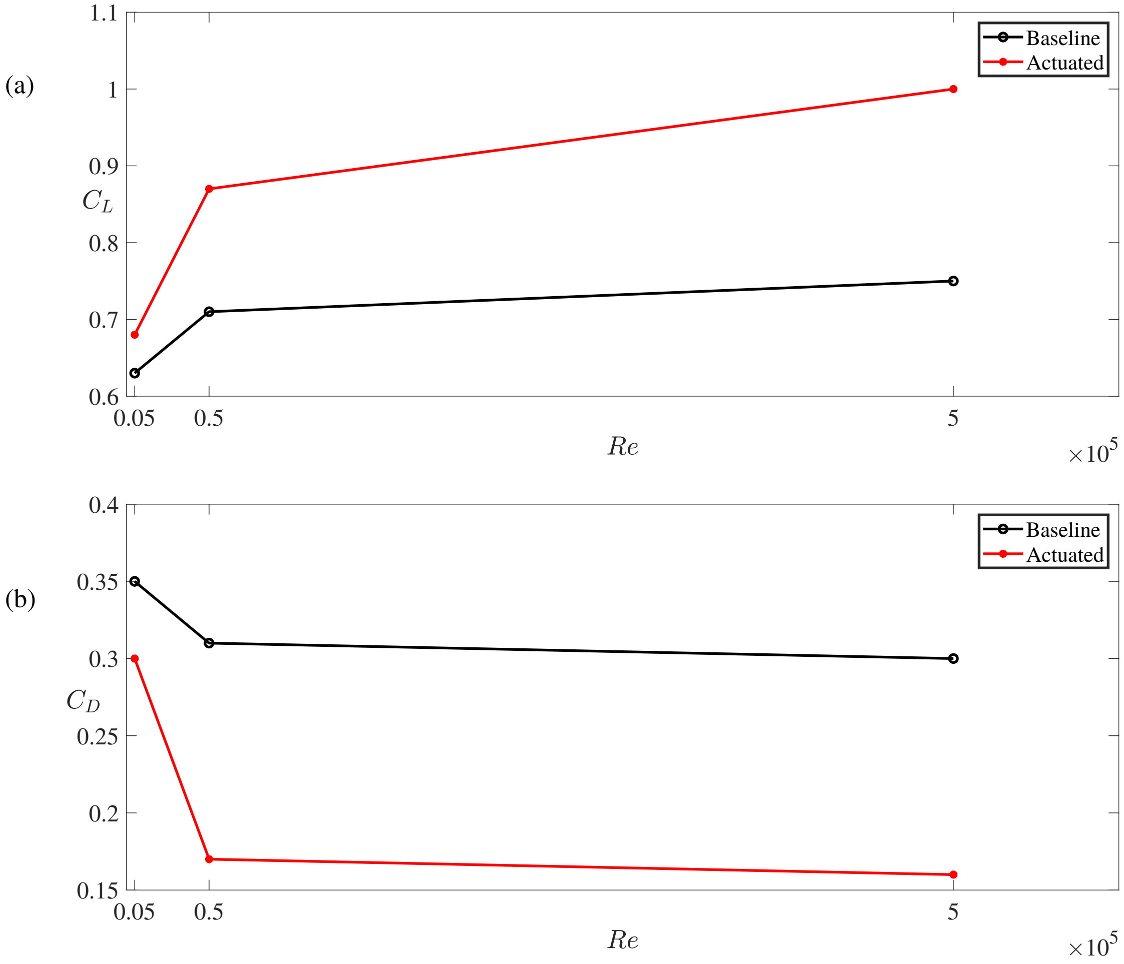

Fig. 3 Plots of the (a) lift (C_L) and (b) drag (C_D) profiles of the baseline and actuated airfoil for $Re = 5,000 - 500,000$.

A. Lift and Drag of Airfoil

From Table 1, the baseline airfoil results of the lift and drag are shown for Reynolds number, $Re = 5,000, 50,000$ and $500,000$ at cases 1, 4^* and 6, respectively. The lift and drag data from Table 1 are plotted in Figures 3a and 3b, respectively. From Figs. 3a and 3b, increasing the Reynolds number from $Re = 5,000$ (cases 1) to $Re = 50,000 - 500,000$ (cases 4^* and 6), the aerodynamic performance (lift enhancement and drag reduction) of the baseline airfoil insignificantly increases as the stall is not suppressed. A low amplitude traveling wave actuation, applied at $Re = 5,000$ and reduced frequencies $f^* = 0.6$ (case 2) and $f^* = 8$ (case 3), insignificantly affects the lift and drag relative to the baseline case 1. The lift and drag are similar to the baseline case 1. Nevertheless, our previous work [9, 16] showed that a low amplitude ($a^* = 0.001$) traveling wave actuation, with frequency $f^* = 8$, applied at AOA=20° and $Re = 50,000$ (case 5^*), significantly increases C_L and significantly decreases C_D by approximately 23% and 54%, respectively, compared to the baseline case 4^*. Increasing the Reynolds number to $Re = 500,000$ (case 7), the traveling wave actuation, with frequency $f^* = 8$, significantly increases C_L and significantly reduces C_D by by 33% and 47%, respectively. This suggests that a backward traveling wave surface morphing actuation of $a^* = 0.001$ and $f^* = 8$ will improve the aerodynamic performance of the airfoil at post-stall angle of attack for $Re = 50,000 - 500,000$.

B. Flow Visualization

The impact of the Reynolds number on the flow control of the actuation on the flow separation around the airfoil for the cases listed in table 1 can be observed by the contours of the instantaneous spanwise vorticity profile around the airfoil NACA0018 at different Re. Figure 4 shows the cycle evolution of the instantaneous spanwise vorticity for both the baseline and actuated cases at $Re = 5,000, 50,000$ and $500,000$. The baseline and actuated cases are visualized at four different phases of the trailing edge vortex shedding cycle. From case 1 at $Re = 5,000$, the laminar boundary layer separates from the leading edge of the airfoil, with a massive vortex at the trailing edge as shown in Fig. 4. The formation and shedding of the vortex at the trailing edge leads to the decrease of the lift and stall of the airfoil. Applying a backward traveling wave actuation with $f^* = 0.6$ and $a^* = 0.001$ in case 2 insignificantly influences the flow separation as the flow field is similar to that of case 1. Increaseing the reduced frequency to $f^* = 8$ (case 3) did not have any significant effect on the flowfield. The flow field and the size of the trailing edge vortex is relatively similar compared to the baseline case 1. This is probably because the flow boundary layer is fully laminar at $Re = 5,000$. On the other hand, for $Re = 50,000$ with no actuation (case 4^*), the boundary layer separates from the leading edge and a

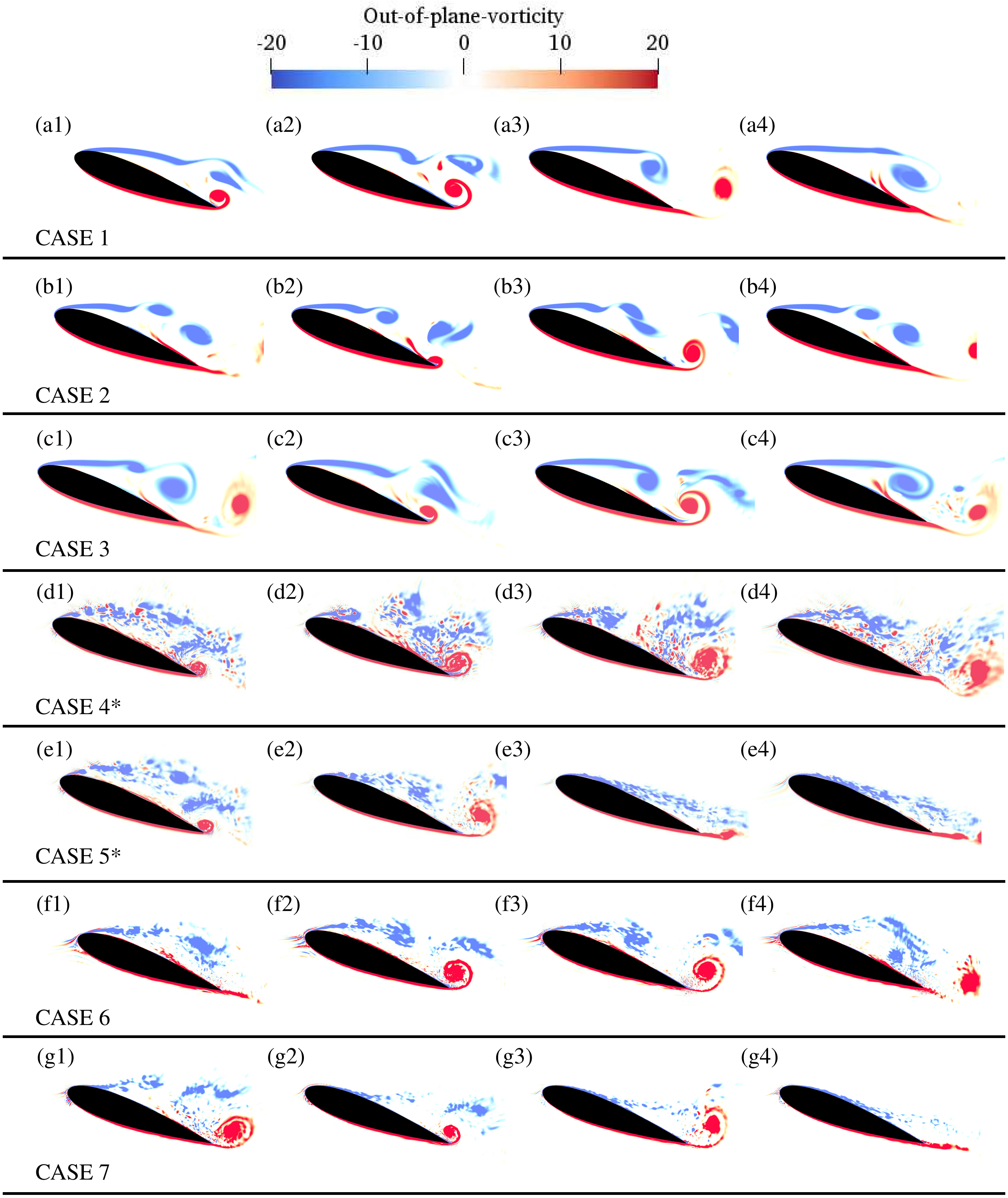

Fig. 4 The contours of the instantaneous out-of-plane vorticity at AOA = 20°.

large reverse zone is generated near the trailing edge. The large vortex is also shed continuously near the trailing edge. Applying a backward traveling wave actuation with $f^* = 8.0$ and $a^* = 0.001$ in case 5^* significantly suppressed the stall such that flow reattachment occurred and the large reverse zone near the trailing edge was eliminated. Significant lift enhancement and drag reduction was also observed as shown in Fig. 3. This suggests that an important mechanism of flow control to suppress the stall is the triggering of the boundary layer instabilities to transition the laminar boundary layer to turbulence [16]. For $Re = 500,000$, cases 6 and 7 represent the baseline and actuated airfoils, respectively. The turbulent boundary layer separated near the leading edge, with a large vortex generated near the trailing edge (case 6). The application of the traveling wave actuation with $f^* = 8.0$ and $a^* = 0.001$ (case 7) significantly reduces the flow separation by reattaching the flow to the upper surface of the airfoil. The stall was suppressed and the large vortex near the trailing edge was eliminated. The flow visualizations, similar to the lift and drag profiles (Fig 3, suggest that a backward traveling wave actuation can significantly suppress the stall and reattach the flow for $Re = 50,000 - 500,000$ at post-stall.

IV. Conclusion

This study investigates and analyzes the effect of Reynolds number on the flow separation control and aerodynamic performance of low amplitude traveling wave surface morphing with at post-stall angle of attack (AOA = 20°) at range of Reynolds number, $Re = 5,000 - 500,000$ using Large-eddy simulations (LES). The influence of backward traveling waves with nondimensional amplitude, $a^* = 0.001$, on the flow separation and aerodynamic performance of a NACA0018 airfoil at different Reynolds number ($Re = 5,000, 50,000,$ and $500,000$) are investigated.

The baseline airfoil experienced flow separation at each Re due to the angle of attack set at the post-stall angle. At $Re = 5,000$, the plots of lift, drag, and the instantaneous spanwise vorticity contours suggest that traveling wave actuation has an insignificant effect on the flow over the baseline airfoil. Nevertheless, significant lift enhancement and drag reduction were achieved at higher Re of $Re = 50,000 - 500,000$ via the application of the traveling wave actuation. The lift increased more than 20% and the drag reduced more than 40% at post-stall relative to the baseline airfoil. The separated flow was reattached to the upper surface of the airfoil at post-stall. Therefore, low amplitude ($a^* = 0.001$) backward traveling wave actuations suppress the stall and reattach the flow at $Re = 5,000 - 500,000$.

Acknowledgments

This work was partly supported by the National Science Foundation (NSF) career grant CBET 1905355. The computational resources were partly provided by the High Performance Research Computing (HPRC) facilities at Texas A&M University.

References

[1] Lissaman, P., "Low-Reynolds-number airfoils," *Annual review of fluid mechanics*, Vol. 15, No. 1, 1983, pp. 223–239. https://doi.org/10.1146/annurev.fl.15.010183.001255.

[2] Greenblatt, D., and Wygnanski, I. J., "The control of flow separation by periodic excitation," *Progress in aerospace Sciences*, Vol. 36, No. 7, 2000, pp. 487–545. https://doi.org/10.1016/S0376-0421(00)00008-7.

[3] Jones, G., Santer, M., Debiasi, M., and Papadakis, G., "Control of flow separation around an airfoil at low Reynolds numbers using periodic surface morphing," *Journal of Fluids and Structures*, Vol. 76, 2018, pp. 536–557. https://doi.org/10.1016/j.jfluidstructs.2017.11.008.

[4] Gerakopulos, R., Boutilier, M., and Yarusevych, S., "Aerodynamic characterization of a NACA 0018 airfoil at low Reynolds numbers," *40th Fluid dynamics conference and Exhibit*, 2010, p. 4629. https://doi.org/10.2514/6.2010-4629.

[5] Kang, W., Lei, P., Zhang, J., and Xu, M., "Effects of local oscillation of airfoil surface on lift enhancement at low Reynolds number," *Journal of Fluids and Structures*, Vol. 57, 2015, pp. 49–65. https://doi.org/10.1016/j.jfluidstructs.2015.05.009.

[6] Shyy, W., Lian, Y., Tang, J., Viieru, D., and Liu, H., *Aerodynamics of low Reynolds number flyers*, Vol. 22, Cambridge University Press, 2008. https://doi.org/10.1017/cbo9780511551154.

[7] Ogunka, U., Akbarzadeh, A., and Borazjani, I., "The Role of Amplitude on Controlling Flow Separation Using Traveling Wave Morphing," *AIAA Scitech 2021*, 2021, p. 2005. https://doi.org/10.2514/6.2021-2005.

[8] Ogunka, U. E., Akbarzadeh, A. M., and Borazjani, I., "Video: Stall Delay of a NACA0018 Airfoil by Traveling Wave Actuations," *74th Annual Meeting of the APS Division of Fluid Dynamics - Gallery of Fluid Motion*, American Physical Society, 2021. https://doi.org/10.1103/aps.dfd.2021.gfm.v0092.

[9] Ogunka, U. E., Akbarzadeh, A., and Borazjani, I., "Flow Control with Traveling-Wave Surface Morphing at Post-Stall Angles of Attack," *AIAA SCITECH 2022 Forum*, 2022, p. 1948. https://doi.org/10.2514/6.2022-1948.

[10] Akbarzadeh, A., and Borazjani, I., “Controlling flow separation on a thick airfoil using backward traveling waves,” *AIAA Journal*, Vol. 58, No. 9, 2020, pp. 3799–3807. https://doi.org/10.2514/1.J059428.

[11] Akbarzadeh, A., and Borazjani, I., “A numerical study on controlling flow separation via surface morphing in the form of backward traveling waves,” *AIAA Aviation 2019 Forum*, 2019, p. 3589. https://doi.org/10.2514/6.2019-3589.

[12] Olivett, A., Corrao, P., and Karami, M. A., “Flow control and separation delay in morphing wing aircraft using traveling wave actuation,” *Smart Materials and Structures*, Vol. 30, No. 2, 2021, p. 025028. https://doi.org/10.1088/1361-665X/abd347.

[13] Thompson, E., and Goza, A., “Surface morphing for aerodynamic flows at low and stalled angles of attack,” *Physical Review Fluids*, Vol. 7, No. 2, 2022, p. 024703. https://doi.org/10.1103/PhysRevFluids.7.024703.

[14] Olivett, A., Corrao, P., and Karami, M., “Flow control and separation delay in morphing wing aircraft using traveling wave actuation,” *Smart Materials, Adaptive Structures and Intelligent Systems*, Vol. 84027, American Society of Mechanical Engineers, 2020, p. V001T06A009. https://doi.org/10.1115/SMASIS2020-2355.

[15] Albers, M., Meysonnat, P. S., and Schröder, W., “Actively reduced airfoil drag by transversal surface waves,” *Flow, Turbulence and Combustion*, Vol. 102, No. 4, 2019, pp. 865–886. https://doi.org/10.1007/s10494-018-9998-z.

[16] Ogunka, U., Akbarzadeh, A., and Borazjani, I., “Mechanisms of Morphing Wall Flow Control by Traveling Waves over a Thick Airfoil (In Press),” *AIAA Journal*, 2022.

[17] Sato, M., Okada, K., Asada, K., Aono, H., Nonomura, T., and Fujii, K., “Unified mechanisms for separation control around airfoil using plasma actuator with burst actuation over Reynolds number range of 103–106,” *Physics of Fluids*, Vol. 32, No. 2, 2020, p. 025102. https://doi.org/10.1063/1.5136072.

[18] Aono, H., Kawai, S., Nonomura, T., Sato, M., Fujii, K., and Okada, K., “Plasma-actuator burst-mode frequency effects on leading-edge flow-separation control at Reynolds number 2.6× 10 5,” *AIAA journal*, Vol. 55, No. 11, 2017, pp. 3789–3806. https://doi.org/10.2514/1.J055727.

[19] Gad-el Hak, M., “The taming of the shrew: why is it so difficult to control turbulence?” *Active flow control*, Springer, 2007, pp. 1–24. https://doi.org/10.1007/978-3-540-71439-2_1.

[20] Sato, M., Asada, K., Nonomura, T., Aono, H., Yakeno, A., and Fujii, K., “Mechanisms for turbulent separation control using plasma actuator at Reynolds number of 1.6× 106,” *Physics of Fluids*, Vol. 31, No. 9, 2019, p. 095107. https://doi.org/10.1063/1.5110451.

[21] Bottom II, R., Borazjani, I., Blevins, E., and Lauder, G., "Hydrodynamics of swimming in stingrays: numerical simulations and the role of the leading-edge vortex," *Journal of Fluid Mechanics*, Vol. 788, 2016, pp. 407–443. https://doi.org/10.1017/jfm.2015.702.

[22] Ge, L., and Sotiropoulos, F., "A numerical method for solving the 3D unsteady incompressible Navier–Stokes equations in curvilinear domains with complex immersed boundaries," *Journal of computational physics*, Vol. 225, No. 2, 2007, pp. 1782–1809. https://doi.org/10.1016/j.jcp.2007.02.017.

[23] Asgharzadeh, H., and Borazjani, I., "A Newton–Krylov method with an approximate analytical Jacobian for implicit solution of Navier–Stokes equations on staggered overset-curvilinear grids with immersed boundaries," *Journal of computational physics*, Vol. 331, 2017, pp. 227–256. https://doi.org/10.1016/j.jcp.2016.11.033.

[24] Balay, S., Buschelman, K., Gropp, W. D., Kaushik, D., Knepley, M. G., McInnes, L. C., Smith, B. F., and Zhang, H., "PETSc Web page," 2001. Http://www.mcs.anl.gov/petsc.

[25] Borazjani, I., Ge, L., and Sotiropoulos, F., "Curvilinear immersed boundary method for simulating fluid structure interaction with complex 3D rigid bodies," *Journal of Computational physics*, Vol. 227, No. 16, 2008, pp. 7587–7620. https://doi.org/10.1016/j.jcp.2008.04.028.

[26] Borazjani, I., and Akbarzadeh, A., "Large Eddy Simulations of Flows with Moving Boundaries," *Modeling and Simulation of Turbulent Mixing and Reaction*, Springer, 2020, pp. 201–225. https://doi.org/10.1007/978-981-15-2643-5_9.

[27] Borazjani, I., Ge, L., and Sotiropoulos, F., "Curvilinear immersed boundary method for simulating fluid structure interaction with complex 3D rigid bodies," *Journal of Computational physics*, Vol. 227, No. 16, 2008, pp. 7587–7620. https://doi.org/10.1016/j.jcp.2008.04.028.

[28] Asadi, H., Asgharzadeh, H., and Borazjani, I., "On the scaling of propagation of periodically generated vortex rings," *Journal of Fluid Mechanics*, Vol. 853, 2018, pp. 150–170. https://doi.org/10.1017/jfm.2018.529.

[29] Ogunka, U. E., Daghooghi, M., Akbarzadeh, A. M., and Borazjani, I., "The Ground Effect in Anguilliform Swimming," *Biomimetics*, Vol. 5, No. 1, 2020, p. 9. https://doi.org/10.3390/biomimetics5010009.

[30] Daghooghi, M., and Borazjani, I., "Self-propelled swimming simulations of bio-inspired smart structures," *Bioinspiration & biomimetics*, Vol. 11, No. 5, 2016, p. 056001. https://doi.org/10.1088/1748-3190/11/5/056001.

[31] Borazjani, I., “Fluid–structure interaction, immersed boundary-finite element method simulations of bio-prosthetic heart valves,” *Computer Methods in Applied Mechanics and Engineering*, Vol. 257, No. 0, 2013, pp. 103–116. https://doi.org/10.1016/j.cma.2013.01.010.

[32] Hedayat, M., and Borazjani, I., “Comparison of platelet activation through hinge vs bulk flow in bileaflet mechanical heart valves,” *Journal of biomechanics*, Vol. 83, 2019, pp. 280–290. https://doi.org/10.1016/j.jbiomech.2018.12.003.

[33] Hedayat, M., Asgharzadeh, H., and Borazjani, I., “Platelet activation of mechanical versus bioprosthetic heart valves during systole,” *Journal of biomechanics*, Vol. 56, 2017, pp. 111–116. https://doi.org/10.1016/j.jbiomech.2017.03.002.

[34] Asgharzadeh, H., Asadi, H., Meng, H., and Borazjani, I., “A non-dimensional parameter for classification of the flow in intracranial aneurysms. II. Patient-specific geometries,” *Physics of Fluids*, Vol. 31, No. 3, 2019, p. 031905. https://doi.org/10.1063/1.5081451.

[35] Asgharzadeh, H., and Borazjani, I., “A non-dimensional parameter for classification of the flow in intracranial aneurysms. I. Simplified geometries,” *Physics of Fluids*, Vol. 31, No. 3, 2019, p. 031904. https://doi.org/10.1063/1.5033942.

[36] Germano, M., Piomelli, U., Moin, P., and Cabot, W. H., “A dynamic subgrid-scale eddy viscosity model,” *Physics of Fluids A: Fluid Dynamics*, Vol. 3, No. 7, 1991, pp. 1760–1765. https://doi.org/10.1063/1.857955.

[37] Rizzetta, D. P., Visbal, M. R., and Morgan, P. E., “A high-order compact finite-difference scheme for large-eddy simulation of active flow control,” *Progress in Aerospace Sciences*, Vol. 44, No. 6, 2008, pp. 397–426. https://doi.org/10.1016/j.paerosci.2008.06.003.

[38] Akhavan-Safaei, A., Seyedi, S. H., and Zayernouri, M., “Anomalous features in internal cylinder flow instabilities subject to uncertain rotational effects,” *Physics of Fluids*, Vol. 32, No. 9, 2020, p. 094107. https://doi.org/10.1063/5.0021815.

[39] Akbarzadeh, A., and Borazjani, I., “Reducing flow separation of an inclined plate via travelling waves,” *Journal of Fluid Mechanics*, Vol. 880, 2019, pp. 831–863. https://doi.org/10.1017/jfm.2019.705.

[40] Akbarzadeh, A. M., and Borazjani, I., “Large eddy simulations of a turbulent channel flow with a deforming wall undergoing high steepness traveling waves,” *Physics of Fluids*, Vol. 31, No. 12, 2019, p. 125107. https://doi.org/10.1063/1.5131268.